Journal of Materials Chemistry A

PAPER

View Article Online
View Journal | View Issue

Cite this: J. Mater. Chem. A, 2016, 4, 7341

Toward environmentally compatible molecular solar cells processed from halogen-free solvents†

Mahmoud E. Farahat,[abc] Cheng-Si Tsao,[de] Yu-Ching Huang,[d] Sheng Hsiung Chang,[f] Widhya Budiawan,[abc] Chun-Guey Wu[f] and Chih-Wei Chu*[c]

Received 15th February 2016
Accepted 4th April 2016

DOI: 10.1039/c6ta01368f

www.rsc.org/MaterialsA

Replacing toxic halogenated solvents with eco-friendly solvents will be necessary for the upscaling and mass production of organic photovoltaics (OPVs). In this study, toluene (Tol), a halogen-free solvent, was employed in the fabrication of molecular solar cells, achieving a power conversion efficiency (PCE) higher than that obtained when using a chlorinated counterpart, chloroform (CF). SMPV1, a two-dimensional conjugated small molecule, was used as the donor and [6,6]-phenyl-C_{71}-butyric acid methyl ester ($PC_{71}BM$) as the acceptor to form bulk heterojunction (BHJ) OPVs. The as-cast device formed using Tol displayed a PCE of 5.4%, higher than that (4.8%) achieved using CF. Combining the effects of thermal annealing and polydimethylsiloxane (PDMS) as a solvent additive, the PCEs of devices prepared using Tol and CF reached 6.20 and 5.52%, respectively. Solvent vapor annealing (SVA), a powerful tool for controlling the morphology of the active layer, had a great impact on the device performance. Tol, tetrahydrofuran (THF), carbon disulphide (CS_2), and hexane (Hex) were tested as halogen-free solvents for SVA treatment. Tol- and THF-SVA had positive effects on PCEs, reaching 7.04 and 6.50%, respectively. The enhancement arose mainly from the improvement in the fill factor, due to morphological manipulation and favorable phase separation. CS_2- and Hex-SVA treatment had negative effects on the short-circuit current density and, hence, the overall PCE. A PCE of greater than 7% is the highest performance reported to date when using a halogen-free solvent to prepare small-molecule solar cells.

Introduction

Light weight, low cost, flexibility, and solution-processability are among the most attractive features of organic photovoltaics (OPVs). Efforts over the last decade to develop reliable and renewable energy technologies have led to several records being set for power conversion efficiencies (PCEs). The PCEs of molecular bulk heterojunction (BHJ) solar cells have reached 10% for single-junction devices—similar to those achieved for polymer BHJ solar cells.[1,2] A PCE of greater than 10% is considered the threshold deemed viable for the commercial adoption of OPVs. For commercial applications, large-scale coating and printing techniques (*e.g.*, roll-to-roll) are compatible with the production of OPVs because they are amenable to solution-processing.[3] Un fortunately, most high-performance OPVs have been prepared using halogenated solvents [*e.g.*, chloroform (CF)[1,4,5] and chlorobenzene[2,6]] because they impart good solubility. Halogenated solvents are, however, an obstacle in the path toward industrialization of OPVs because of their high toxicity. In addition, they are not naturally available and are expensive and energy-intensive to produce, use, and remove as waste. Therefore, there is an urgent need to develop methods to process OPVs from more eco-friendly solvents; in particular, to find greener alternatives to these halogenated counterparts.[7] The use of any such alternative solvents should, however, occur with retention of high device performance (*i.e.*, similar to those obtained using halogenated counterparts). In addition, solvents with medium-temperature boiling points are favored to simplify device fabrication.[8] In this regard, many attempts have been made in recent years to find environmentally friendly solvents to fabricate the active layers in both polymer- and small molecule-based OPVs. For polymer-based OPVs, several halogen-free solvents—including xylenes,[9–12] toluene (Tol),[13] *N*-methyl-2-pyrrolidone (NMP) and its derivatives,[8] trimethylbenzene (TMB),[14,15] anisole,[16] and 2-methylanisole (MA)[17]—have been tested. Other studies have examined the use of halogen-free solvent mixtures, including carbon disulfide (CS_2)/acetone,[18]

[a]Department of Engineering and System Science, National Tsing-Hua University, Hsinchu 30013, Taiwan
[b]Nanoscience and Technology Program, Taiwan International Graduate Program, Academia Sinica and National Tsing-Hua University, Taiwan
[c]Research Center for Applied Sciences, Academia Sinica, Taipei 115, Taiwan. E-mail: gchu@gate.sinica.edu.tw
[d]Institute of Nuclear Energy Research, Longtan, Taoyuan, 32546, Taiwan
[e]Department of Materials Science and Engineering, National Taiwan University, Taipei 10617, Taiwan
[f]Research Center for New Generation Photovoltaics, Jhongli, 32001, Taiwan

† Electronic supplementary information (ESI) available. See DOI: 10.1039/c6ta01368f

acetophenone/mesitylene,[19] and Tol/indane and *o*-xylene/indane.[20] Halogen-free solvents mixed with halogenated solvents have also been examined (*e.g.*, CF/indane,[20] chlorobenzene/*o*-xylene, chlorobenzene/cyclohexane, and chlorobenzene/acetone[21]). On the other hand, few attempts have been made to employ non-halogenated solvents in the fabrication of small molecule-based OPVs. Bazan *et al.*[22] and Brabec *et al.*[23] used the green solvent 2-methyltetrahydrofuran (2-MeTHF) and a halogen-free solvent mixture (benzaldehyde/mesitylene), respectively, in the preparation of molecular OPVs.

Good solubility of organic materials (polymers, small molecules, and fullerenes) in halogen-free solvents is a basic requirement for using such solvents in the fabrication of OPVs. Because of their lower molecular weights, small molecules generally have much better solubility in these solvents than do their polymeric counterparts. This phenomenon is a strong motivation for moving toward using halogen-free solvents in the processing of small molecule-based solar cells.[23,24] To date, one of the highest PCEs achieved when using a halogen-free solvent has been 9.5%, when employing the polymer PffBT4T-2OD as the donor and $PC_{71}BM$ as the acceptor in *o*-xylene containing 1% anisaldehyde as a solvent additive.[11] Recently, Hou *et al.* reported one of the highest PCEs in the polymer-blend system using a single eco-friendly solvent, MA, achieving a PCE of 9.6%.[17] The highest known PCE was achieved by using hydrocarbon-based solvents with performance reaching 11.7%.[15] Li *et al.* prepared a device featuring a P3HT/ICBA blend system that, when cast from Tol containing 2% NMP as a solvent additive displayed a PCE of 6.6%.[13] Jen *et al.* obtained a PCE of 7.2% from a device based on a polymer/fullerene blend system (PIDTT-DFBT : $PC_{71}BM$), prepared using TMB as the solvent containing 2.5% dimethylnaphthalene as a solvent additive.[14] When processed from a halogen-free solvent mixture of benzaldehyde and mesitylene, a device incorporating the small molecule N(Ph-2T-DCN-Et)$_3$ and $PC_{71}BM$ achieved a PCE of 3.7%, comparable with that achieved using chlorobenzene (3.4%).[23] The highest PCE achieved for a small molecule-based OPV, 5%, was obtained after processing with the green solvent 2-MeTHF.[22] Tables S1 and S2 (ESI†) provide partial lists of the halogen-free solvents and mixtures that have been used in the preparation of devices based on polymers and small molecules, respectively, with device performance data also provided for comparison.

The active layer morphology is mainly determined from the interactions among the donor, acceptor, and solvent during the film drying process or from the interactions between the donor and acceptor in the solid state during annealing or post-treatment processes.[24,25] Accordingly, thermal annealing,[26] the use of solvent additives,[27,28] and solvent vapor annealing (SVA)[29–34] are common strategies for manipulating the active layer morphology in BHJ OPVs. In the SVA process, the vapor of the solvent penetrates into the active layer blend, avoiding any direct contact of the bulk liquid solvent with the active layer. Organic molecules in the active layer dissolve locally and become more mobile upon exposure to the saturated vapor of the solvent. As a result, molecules in the active layer reorganize, allowing the system to evolve toward morphologies in a lower-energy state, leading to a higher structural order in the active layer.[35,36]

In this study, we report an efficient molecular photovoltaic device incorporating low-bandgap small-molecule materials: SMPV1 (ref. 37) as the donor and $PC_{71}BM$ as the acceptor. We processed the active layers from Tol, *m*-xylene, and TMB as halogen-free host solvents and CF as a halogenated solvent. Devices fabricated from Tol, without additives or post-treatment, displayed PCEs higher than those of devices prepared using the other tested halogen-free solvents. A device prepared using Tol achieved a PCE of 5.39%; in comparison, we measured a value of 4.83% for a device prepared using CF under otherwise identical conditions. Combining the effects of polydimethylsiloxane (PDMS; 0.5 mg mL^{-1}) as a solvent additive and thermal annealing (at 80 °C for 10 min) enhanced the PCEs significantly; a device fabricated using Tol reached a PCE of 6.20%, while that processed from CF reached 5.52%. For further device optimization, we applied SVA using various halogen-free solvents: Tol, THF, CS_2, and Hex. Active layers cast from Tol containing PDMS (0.5 mg mL^{-1}) and thermally annealed at 80 °C for 10 min were subjected to SVA under various solvents, followed by Ca/Al cathode deposition to complete the devices. A device exposed to Tol-SVA exhibited the best device performance, with its PCE of 7% arising mainly from a significant enhancement in the fill factor (FF), which increased from 53.8% for the device prepared without SVA to 63.0% for the devices prepared with Tol-SVA. THF-SVA had a similar effect on the FF, leading to an increase of PCE to 6.51%. Both CS_2- and Hex-SVA had adverse effects on the short-circuit current density (J_{sc}), resulting in the decrease of PCEs to 5.63 and 5.56%, respectively. To the best of our knowledge, the PCE of 7% reported herein is the highest achieved for a small molecule-based OPV fabricated using halogen-free solvents.

Experimental section

Materials and solution preparation

The low-bandgap small molecular material SMPV1 (purity > 99.9%) was obtained from Luminescence Technology (Lumtec). $PC_{71}BM$ was purchased from Solenne b.v. The conducting polymer poly(3,4-ethylenedioxythiophene)/polystyrenesulfonate (PEDOT : PSS) was obtained from Clevios PVP 4083. The solvent additive PDMS was purchased from Alfa Aesar. Solutions containing SMPV1 at various concentrations (10, 15, and 20 mg mL^{-1}) at a SMPV1 : $PC_{71}BM$ ratio of 1 : 0.75 were prepared in Tol in the presence of various amounts of PDMS. Solutions with SMPV1 : $PC_{71}BM$ ratios of 1 : 0.5, 1 : 0.75, 1 : 0.85, and 1 : 1 were also prepared. All solutions were heated at 70 °C in a glovebox for 3 h prior to use. Tol, THF, CS_2, and Hex were purchased from Sigma-Aldrich.

Device fabrication

Devices were fabricated on 0.1 cm^2 pre-patterned indium tin oxide (ITO)-coated glass substrates (sheet resistance < 8 Ω per square) with the conventional device structure ITO/PEDOT : PSS/SMPV1 : $PC_{71}BM$/Ca/Al. Prior to device fabrication, the ITO-coated glass substrates were cleaned using standard procedures: sonication in detergent, acetone, and

isopropyl alcohol; rinsing in deionized (DI) water; and treating with UV/ozone for 15 min. The solution of PEDOT : PSS was passed through a 0.45 μm syringe filter onto the clean substrates, which were then spin-coated (4000 rpm, 60 s) and annealed in air for 30 min at 130 °C, forming a thin film (thickness: 40 nm). The active layer solution was then spin-coated at various speeds for 60 s within a glovebox filled with N_2. Post-deposition treatment was applied to the active layer prior to cathode deposition: thermal annealing at various annealing temperatures and for various lengths of time, or SVA treatment using various solvents, temperatures, and annealing periods. SVA treatment was applied after the deposition of the active layer by exposing the films to the saturated vapor of a solvent in a closed Petri dish (diameter: 30 mm). Finally, the Ca (20 nm) and Al (80 nm) cathode was deposited through thermal evaporation in a vacuum chamber (6×10^{-6} torr).

Device characterization

The photovoltaic performance of each device was measured inside a glovebox filled with N_2 under simulated AM 1.5 G illumination (100 W cm^{-2}) using a Xe lamp-based solar simulator (Thermal Oriel 1000 W). The light intensity was calibrated using a mono-silicon photodiode featuring a KG-5 color filter (Hamamatsu). EQE spectra were recorded using a QE-R apparatus (Enlitech) operating in the AC mode. The devices were encapsulated within a glovebox filled with N_2 prior to removal for the EQE measurements. The absorption spectra of the films were measured using a Jacobs V670 UV-Vis-NIR spectrophotometer. A Bruker Innova atomic force microscope (Digital Instrument NS 3a controller equipped with a D3100 stage) was used, in the tapping mode, to record the surface morphologies of the active layers. For TEM (JEM 2100F) characterization, the active layer on the PEDOT : PSS substrate was removed by dipping in DI water and then a holey carbon-coated copper grid (Ultrathin Carbon Type A, 400 mesh, Copper; TED Pella) was used to hold the film, which was dried in an oven at 50 °C. PL spectra were recorded using a fluorescence spectrophotometer (F-4500, Hitachi, Tokyo, Japan) with a Xe lamp operating at 150 W as the excitation source at an excitation wavelength of 405 nm. The configurations of the hole- and electron-only devices were ITO/PEDOT : PSS/small molecule : $PC_{71}BM/V_2O_5$/Al and ITO/Cs_2CO_3/small molecule : $PC_{71}BM$/Ca/Al, respectively. The electron and hole motilities were determined by fitting the plots of the dark *J–V* curves for single-carrier devices to the SCLC model.[38] Simultaneous GISAXS and GIWAXS measurements of all SMPV1 : PCBM blend films were performed at beam-line 23A of the National Synchrotron Radiation Research Center (NSRRC), Taiwan. In the GISAXS/GIWAXS measurements, the incident angle to each thin film was aligned precisely to 0.2 ± 0.002°, allowing penetration through the whole active layer. Two-dimensional (2D) GISAXS and GIWAXS patterns were collected simultaneously from two 2D detectors located at different positions.[39,40] The thin films for GISAXS and GIWAXS measurements were deposited on PEDOT : PSS-coated silicon wafers. The 2D patterns of the scattering profiles were expressed as a function of the scattering vector *Q*.

Results and discussion

Fig. 1(a) displays the chemical structures and energy levels of SMPV1 and $PC_{71}BM$, which we used to form the active layers in this study. Fig. 1(b) and (c) present the chemical structures of the halogen-free solvents tested as host solvents (Tol, *m*-xylene, TMB) and used for SVA treatment (Tol, THF, CS_2, Hex), respectively. Yang *et al.* were the first to introduce SMPV1 as a small molecule for use in organic solar cells. In their pioneering study, they processed SMPV1/$PC_{71}BM$ active layers from CF, a halogenated solvent, with and without PDMS as a solvent additive. They achieved a PCE of 7.2% in the absence of PDMS and a value of 8.1% when adding PDMS at 0.5 mg mL^{-1}.[37] Commercial SMPV1-based devices fabricated using CF containing PDMS (0.5 mg mL^{-1}) as the solvent, but otherwise under identical conditions, reached a PCE of only 5.53%.[41] In our present study, the as-cast device fabricated from CF achieved a PCE of 4.83% without any treatment and 5.52% when combining the effects of thermal annealing and the application of PDMS (0.5 mg mL^{-1}) as an additive. We also tested Tol, *m*-xylene, and TMB as eco-friendly halogen-free solvents, as potential substitutes for CF, while still achieving PCEs close to those obtained by Yang *et al.* Fig. 2(a) and Table 1 present the photovoltaic characteristics of devices processed using the various halogen-free solvents, relative to those obtained using CF as the halogenated solvent. The devices processed using Tol, among all the solvents examined, exhibited the best device performance. After optimization (ESI;† Fig. S1–S4 and Tables S3–S6), we obtained an SMPV1 : $PC_{71}BM$ device, fabricated using Tol as the solvent, without any subsequent treatment (*i.e.*, as-cast) that displayed a PCE of 5.39%, compared with a value of 4.83% for the corresponding CF-processed device [Table 1 and Fig. 2(a)]. The synergistic effects of both thermal annealing and the use of PDMS as an additive (hereafter, the "controlled conditions") led to significant enhancements in the PCEs of devices processed from both Tol and CF [Fig. 2(b)]. The Tol-processed device provided a PCE of 6.20%, with a significant enhancement in the value of J_{sc} from 10.68 (for the as-cast device) to 12.13 mA cm^{-2} (for the control device). The same trend occurred for the device processed from CF, but its PCE (5.52%) remained lower than that of the Tol-processed device.

The AFM surface morphology (tapping mode) of active layers processed from CF, Tol, *m*-xylene and TMB without any post-treatment (as-cast) has been shown in Fig. 3. The effect of changing the processing solvent on the surface morphology is clearly shown. The surface morphology of active layers processed from CF and Tol is similar without obvious changes due to the solvent change [Fig. 3(a) and (b)]. A slight difference in the root-mean-square (rms) roughness has been noticed for CF and Tol with values of 0.90 and 0.74 nm, respectively. However, for active layers processed from *m*-xylene and TMB shown in Fig. 3(c) and (d) respectively, RMS showed a significant increase to 1.73 for *m*-xylene 2.31 nm for TMB. Both *m*-xylene and TMB showed noticeable changes in the surface morphology of the active layers relative to Tol. This might be a reason why Tol showed the best performance compared to *m*-xylene and TMB as halogen-free solvents.

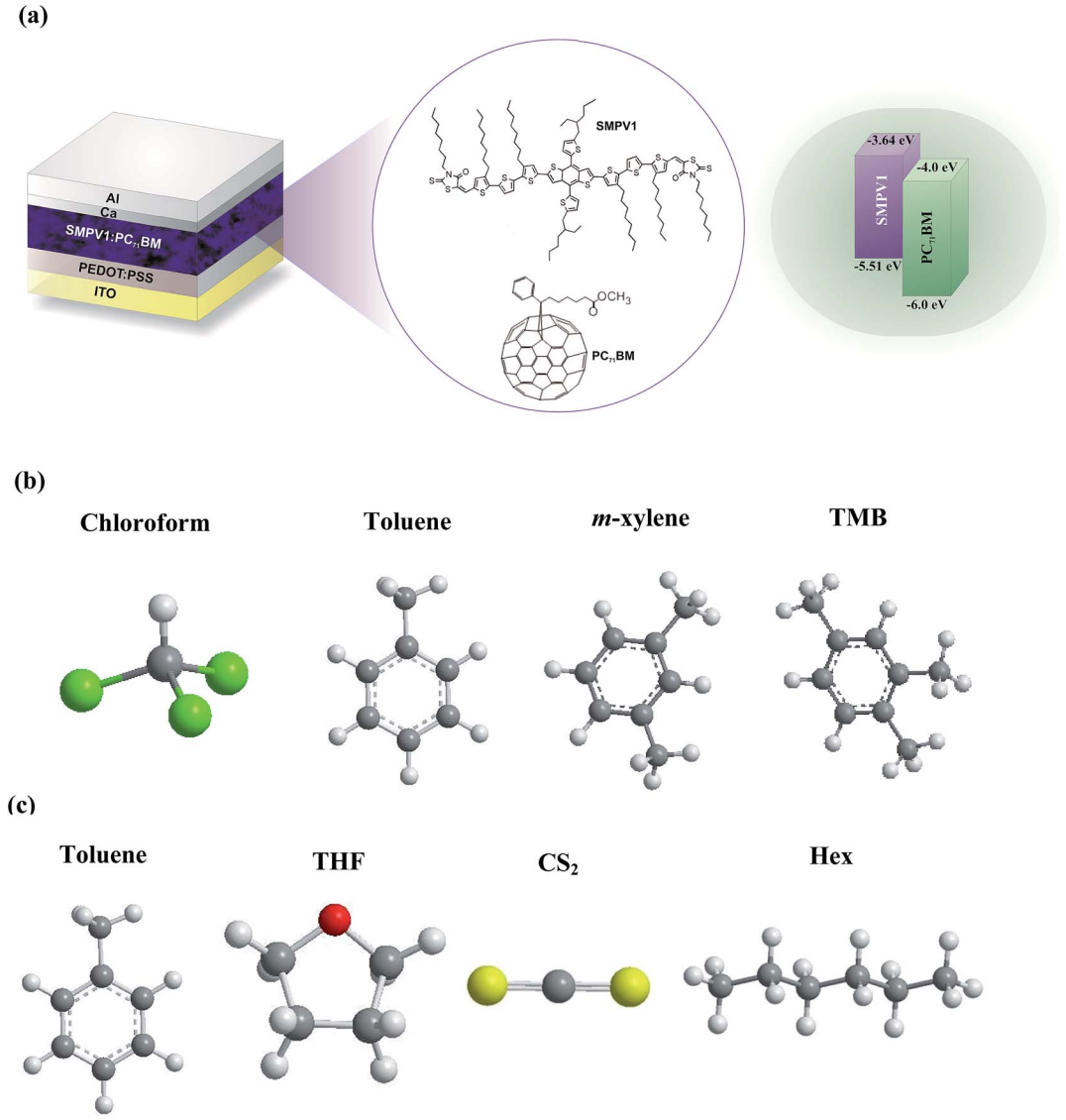

Fig. 1 (a) Chemical structures of SMPV1 and $PC_{71}BM$ and their energy levels. (b) Halogen-free host solvents used to dissolve the organic materials. (c) Halogen-free solvents used for SVA treatment.

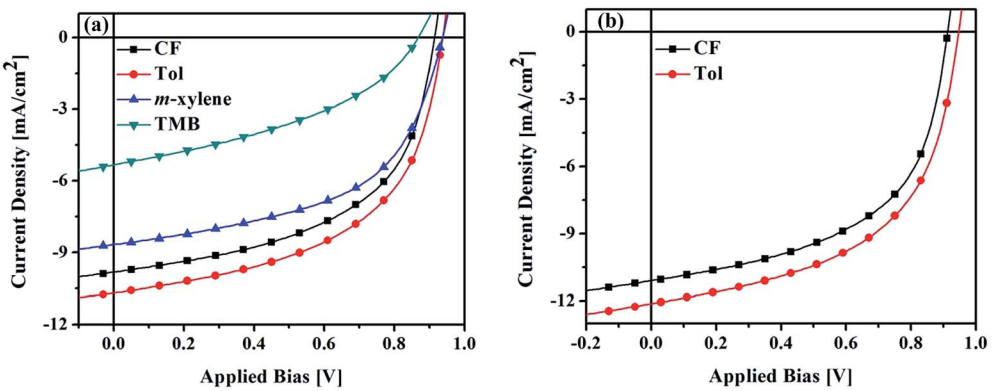

Fig. 2 *J–V* photovoltaic characteristics of SMPV1 : $PC_{71}BM$ devices processed from halogen-free solvents, compared with those obtained through processing with CF as the halogenated solvent, (a) without any additive and (b) with PDMS (0.5 mg mL^{-1}) in Tol and CF.

Table 1 Photovoltaic characteristics of SMPV1 : $PC_{71}BM$ devices processed from halogen-free solvents, compared with those processed using CF, in the absence and presence of the additive PDMS (0.5 mg mL^{-1})

Solvent	PDMS additive	Thermal Ann.	J_{sc} [mA cm^{-2}]	V_{oc} [V]	FF [%]	PCE [%]
CF	No	No	9.80	0.91	54.16	4.83
Tol	No	No	10.68	0.94	53.69	5.39
m-Xylene	No	No	8.66	0.94	53.31	4.34
TMB	No	No	5.32	0.87	39.97	1.85
CF	0.5 mg mL^{-1}	80 °C, 10 min	11.08	0.91	54.75	5.52
Tol	0.5 mg mL^{-1}	80 °C, 10 min	12.13	0.95	53.80	6.20

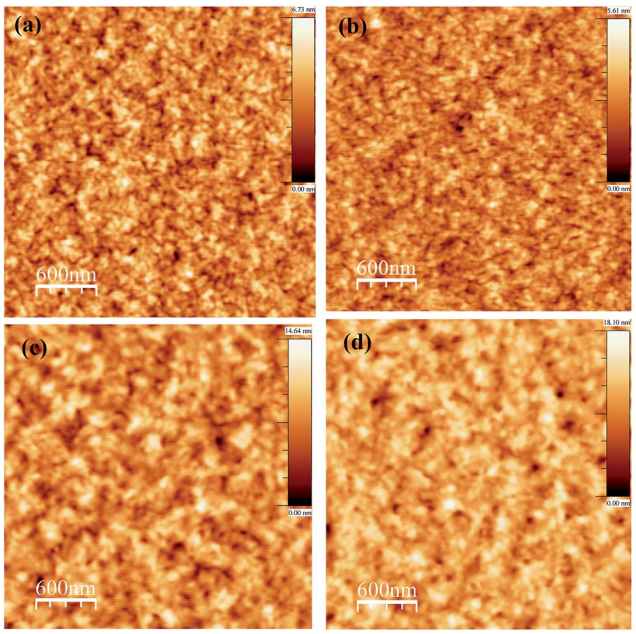

Fig. 3 AFM height images of the as-cast SMPV1 : $PC_{71}BM$ active layers processed from (a) CF, (b) Tol (c) *m*-xylene and (d) TMB.

To continue the optimization process, we processed the active layers, obtained under the controlled conditions, through SVA treatment using various halogen-free solvents (Tol, THF, CS_2, and Hex) prior to Ca/Al deposition. SVA treatment significantly improved the photovoltaic performance of the resulting devices [Fig. 4(a); Table 2]. Because Tol-SVA treatment provided the best device performance, we performed a series of optimization experiments (see Fig. S5 and S6 and Tables S7–S9, ESI†). The device prepared using Tol-SVA for 60 s exhibited a J_{sc} value of 12.55 mA cm^{-2} and an FF of 63%, leading to a PCE of 7%—the highest reported for a device based on small molecules cast from a halogen-free solvent. The same trend occurred when applying THF-SVA for 30 s: the PCE increased to 6.5% with a significantly improved FF of 63.34%. Although CS_2 SVA (45 s) enhanced the FF to 60.10%, it adversely affected the value of J_{sc} and resulted in a PCE (5.63%) lower than that of the device prepared under the controlled conditions. Hex was the only SVA solvent that decreased the FF; in addition, it had a negative effect on the value of J_{sc}, leading to a PCE of 5.56%. All of the other solvents tested for SVA significantly enhanced the FFs, suggesting that they all enhanced the crystallinity of SMPV1 inside the active layer.[42] We calculated the series resistance (R_s) and shunt resistance (R_{sh}) of the OPV devices to investigate the effects of SVA treatment on their FFs. Table 2 shows that the values of R_s decreased after SVA with Tol, THF, and CS_2, accompanied by significant increases in the values of R_{sh}—an indication that SVA treatment led to suppression of the leakage current.[31] We observed decreases in the open-circuit voltages (V_{oc}) of the devices subjected to SVA with Tol, THF, and CS_2. The value of V_{oc} is defined mainly by the difference in energy between the highest occupied molecular orbital (HOMO) of the donor (SMPV1) and the lowest unoccupied molecular orbital (LUMO) of the acceptor ($PC_{71}BM$). SVA positively influenced the crystallinity of the SMPV1 molecules and $PC_{71}BM$ domains in the active layer. Consequently, the number of delocalized electrons increased upon increasing the crystallite sizes, leading to a decrease in the energy difference between the HOMO of SMPV1 and the LUMO of $PC_{71}BM$ and, hence, a decrease in the value of V_{oc}.[25,32]

The enhancements in the values of J_{sc} after SVA treatment with the various solvents were recorded through measurements of external quantum efficiencies [EQEs; Fig. 4(b)]. Compared with the devices processed under the as-cast and controlled conditions, the Tol- and THF-SVA-treated devices exhibited broad photoresponses over the entire photoresponsive range from 300 to 700 nm. The EQE peaks of the Tol- and THF-SVA-treated devices reached 65.5 and 61.0%, respectively, at 550 nm. For the CS_2- and Hex-SVA-treated devices, we observed decreases in the intensities of the EQE signals over the entire range of wavelengths, consistent with their lower values of J_{sc} mentioned above. Fig. 4(c) presents the UV-Vis absorption spectra of the active layers prepared under the same treatment conditions as those discussed above for device performance. The absorption spectra of active layers subjected to various treatment conditions can provide information regarding the molecular ordering of their components. For the as-cast active layer, the absorption range stretched from 300 to 700 nm, with four absorption peaks. One peak at 476 nm, the absorption maximum at 570 nm, and a weak shoulder at 630 nm were all provided by SMPV1; $PC_{71}BM$ contributed the fourth absorption peak, at 377 nm. Compared with the as-cast film, the active layer formed under the controlled conditions revealed increased absorption intensities, combined with red-shifts and pronounced vibronic peaks. After Tol- and THF-SVA, the

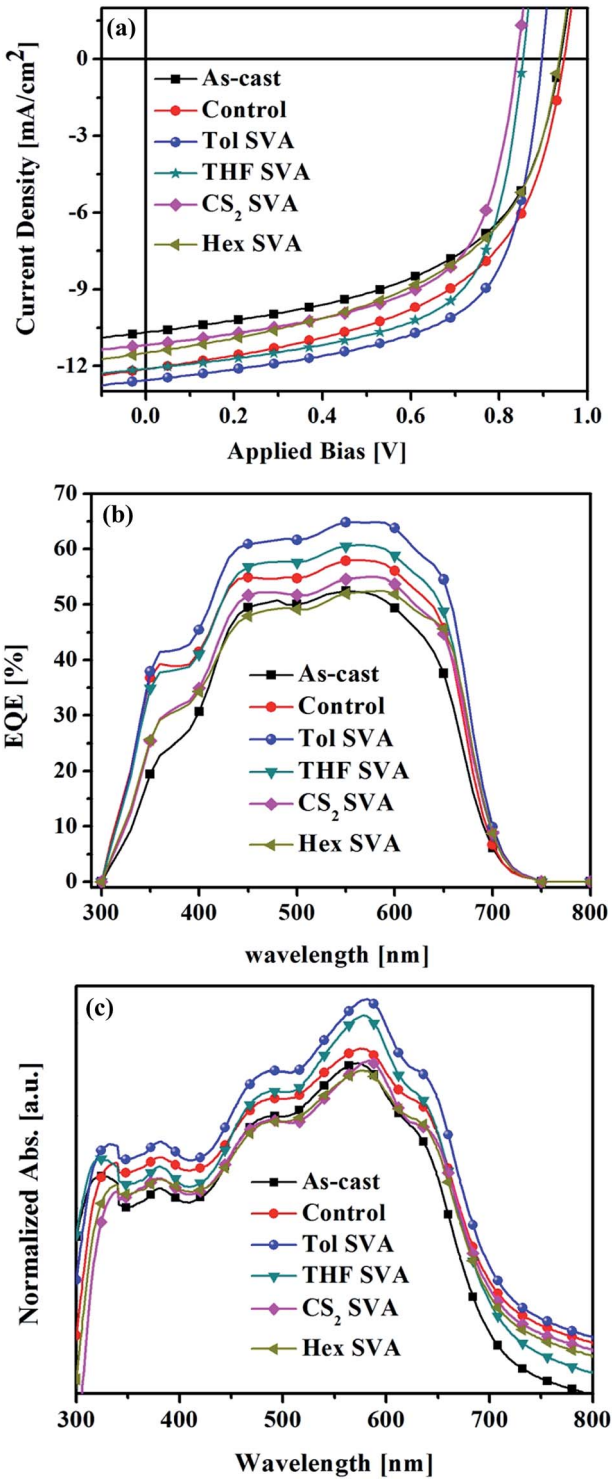

Fig. 4 (a) J–V photovoltaic characteristics of SMPV1 : $PC_{71}BM$ devices processed from Tol and subjected to SVA using various treatment solvents. (b) Corresponding EQE and (c) UV-Vis absorbance spectra of active layers prepared under the same conditions.

intensities of the signals of the active layer increased with greater red-shifting relative to those of the as-cast and control devices. The shoulder at 630 nm red-shifted to 644 nm after Tol-SVA and to 635 nm after THF-SVA, with well-defined features. A red-shift in the absorption peak is indicative of an ordered structure in an active layer morphology.[43] We attributed the increases in the intensity of the shoulder signals at 644 and 635 nm, after Tol- and THF-SVA, respectively, to enhanced π–π stacking and intermolecular interactions in the donor phase.[44,45] Such interactions are one reason behind the enhanced values of J_{sc} and FF of the devices prepared using the Tol- and THF-SVA conditions. Although the CS_2- and Hex-SVA-treated films did not feature any changes in intensity in their absorption profiles, their signals were slightly red-shifted relative to those of the as-cast films. This phenomenon is indicative of unfavorable morphological changes in the films subjected to CS_2- and Hex-SVA, consistent with their poorer device performances. From the UV-Vis absorption profiles, we conclude that SVA had a powerful effect on the crystallinity and morphology of the active layers and, therefore, on the device performance. Heeger *et al.* reported a drop in the value of V_{oc} after using a solvent additive to enhance the donor crystallinity in the active layer; they attributed this behavior to stronger molecular interactions arising through better crystallization.[46] From our present results, we ascribed the observed decreases in the values of V_{oc} after SVA to the enhanced π–π stacking and intermolecular interactions occurring in the donor phase.

To understand the effect of SVA on the device performance we used AFM (tapping mode) to investigate the morphology of active layers of SMPV1 : $PC_{71}BM$ under various treatments. Fig. 5 shows the height images of active layers all processed from Tol under controlled conditions (a), Tol-SVA (b), THF-SVA (c), CS_2-SVA (d) and Hex-SVA (e) and the corresponding phase images are shown in Fig. S7 (ESI†). Active layers subjected to SVA featured a significant difference in the morphological order relative to the active layers formed under the controlled conditions. The films that had been subjected to Tol- and THF-SVA [Fig. 5(b) and (c), respectively] featured a more uniform morphology and better donor/acceptor interpenetrating network compared to the active layers obtained without SVA (controlled conditions). An increase in rms roughness after Tol- and THF-SVA to 1.20 and 1.14 nm, respectively, has been observed compared to that of the active layer formed under the controlled conditions (rms = 0.80 nm). With Tol- and THF-SVA we were able to manipulate the morphology of active layers in a way to obtain the favored donor/acceptor aggregation size benefited charge transfer and separation. Fig. 5(d) and (e) display the active layer morphologies of films subjected to CS_2- and Hex-SVA treatment, with an rms roughness of 0.93 and 0.90 nm, respectively. Although the FF of the device prepared using CS_2-SVA was higher (60%) than that of the control device, it had a lower value of J_{sc}, leading to a lower PCE of 5.6%. We suspect that the moderate solubility of the donor phase in CS_2 led to this solvent vapor having lower ability to penetrate into the active layer. Similarly, SMPV1 has limited solubility in Hex, and, thus, we observed no change in the FF after Hex-SVA treatment. Although both CS_2- and Hex-SVA treatments led to noticeable changes in the morphologies relative to those of the control device, these morphologies were quite close to those of the as-cast film.

Table 2 Photovoltaic characteristics of SMPV1 : $PC_{71}BM$ devices processed from Tol and subjected to SVA using various treatment solvents

Condition	SVA duration [s]	J_{sc} [mA cm^{-2}]	V_{oc} [V]	FF [%]	PCE [%]	R_s [Ω cm^2]	R_{sh} [kΩ cm^2]
As-cast (Tol)[a]	—	10.68	0.94	53.69	5.39	7.01	0.40
Control (Tol)[b]	—	12.13	0.95	53.80	6.20	5.37	0.61
Tol-SVA[b]	60	12.55	0.89	63.03	7.04	2.71	1.30
THF-SVA[b]	30	12.11	0.85	63.34	6.52	2.85	1.12
CS_2-SVA[b]	45	11.15	0.84	60.11	5.63	2.78	1.07
Hex-SVA[b]	60	11.48	0.94	51.52	5.56	4.64	0.47

[a] Without additive; without thermal annealing. [b] With PDMS (0.5 mg mL^{-1}) added to Tol solution; with thermal annealing at 80 °C for 10 min.

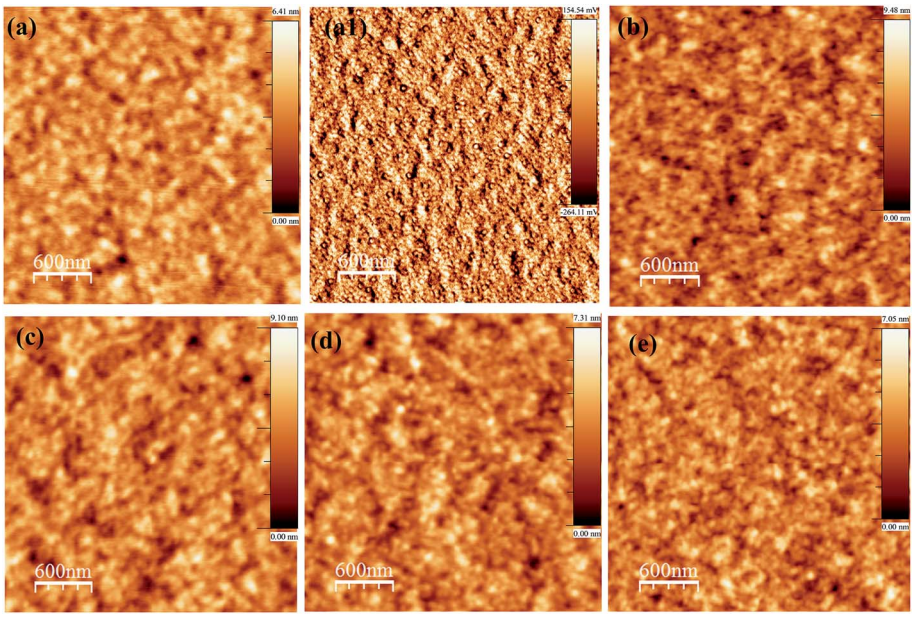

Fig. 5 AFM images of SMPV1 : $PC_{71}BM$ active layers processed from Tol and subjected to SVA using various treatment solvents; (a) control, (b) Tol-SVA, (c) THF-SVA, (d) CS_2-SVA, and (e) Hex-SVA. (a–e) Height images and (a1) corresponding phase images of the control device.

AFM can only observe the surface morphology of the active layers, while TEM can be used to probe the bulk morphology of the films. We recorded TEM images to further confirm the ability of SVA to tune the morphologies of active layers cast from halogen-free solvents (Fig. 6). Similar to the observation in the AFM images, the as-cast film [Fig. 6(a)] exhibits finer features than does the film processed under the controlled conditions [Fig. 6(b)]. The Tol- and THF-SVA-treated films [Fig. 6(c) and (d), respectively] exhibited phase separation and domain sizes larger than those in the as-cast films and smaller than those obtained under the controlled conditions. Films treated with CS_2- and Hex-SVA [Fig. 6(e) and (f), respectively] had domain sizes smaller than those obtained using Tol- and THF-SAV. The morphologies observed in the TEM images are consistent with those recorded using AFM, confirming that SVA can be a powerful tool for tailoring active layer morphologies. Fig. S8 (ESI†) reveals the effect of the various treatment conditions on the photoluminescence (PL) behavior of SMPV1 : $PC_{71}BM$. The film of the pristine SMPV1 donor had its maximum emission peak at 707 nm. For the SMPV1 : $PC_{71}BM$ films, significant quenching of the PL emission occurred under all treatment conditions. There was, however, a clear difference between the quenching capabilities obtained after applying each condition, confirming the tuning of morphologies observed in the AFM and TEM analysis. The Tol- and THF-SVA-treated films exhibited moderate quenching relative to the as-cast (higher PL quenching) and control (lower PL quenching) films. This behavior, together with the AFM and TEM analysis and device performance data, suggested that Tol- and THF-SVA treatment optimized the film morphology and led to efficient device performance.

Three-dimensional self-organized BHJ nanostructures formed through phase separation of organic molecules and fullerenes in the blend films are complicated structures on multiple length scales. The multi-length-scale BHJ structures of the active layers in molecular solar cells[39,47,48] and polymer solar cells[32,40,49–52] have been studied previously using the powerful tools of grazing-incidence small- and wide-angle X-ray scattering (GISAXS and GIWAXS, respectively). In the present study, we used simultaneous GISAXS and GIWAXS to gain insight into

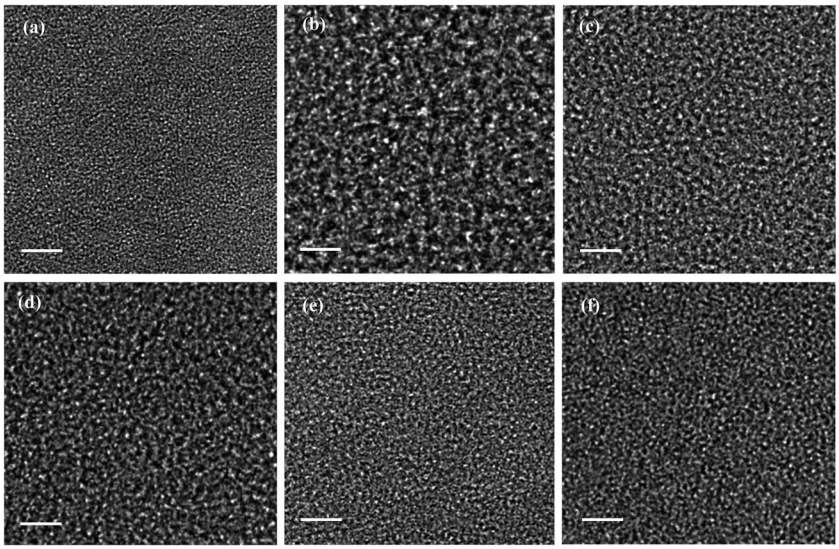

Fig. 6 TEM images of SMPV1 : $PC_{71}BM$ active layers processed from Tol and subjected to SVA using various treatment solvents. (a) As-cast, (b) control, (c) Tol-SVA, (d) THF-SVA, (e) CS_2-SVA, and (f) Hex-SVA films. Scale bar: 200 nm.

the structural evolution of SMPV1 : $PC_{71}BM$ blend films fabricated using Tol as a halogen-free solvent and then tuned using various post-treatment conditions; we also used it to examine the correlation between structure and performance. It has been reported that the π-conjugated SMPV1 molecules can self-assemble into ordered lamellar structures during crystallization.[37] The 2D GIWAXS patterns (Fig. S9, ESI†) of the pristine SMPV1 and SMPV1 : $PC_{71}BM$ blend films featured diffraction spots of the (100) lamellar plane dominating in the out-of-plane direction (*i.e.*, perpendicular to the film surface), indicating the preferred orientation of the small-molecule crystallites. Therefore, the representative 1D GIWAXS profiles can be mainly reduced by a cake cut along the out-of-plane direction, as shown in Fig. 7(a). For the pristine SMPV1 film, the strong peak at a Q value of 5.9 nm^{-1} and the weak peak at a Q value of 8.85 nm^{-1} in the out-of-plane GIWAXS profile are the second- and third-order diffraction peaks, respectively, of the (100) plane of the lamellar structure of crystallites. We estimated that the (100) diffraction peak appearing at a Q value of 2.95 nm^{-1} (*i.e.*, $2\theta = 4.15°$ for the normal XRD peak) corresponds to an interspacing between (100) planes of 21.3 Å, consistent with the reported value.[37] The SMPV1 crystallites had their main orientation with the (100) plane of the lamellar structure perpendicular to the film surface (*i.e.*, edge-on orientation).

In contrast, the 1D GIWAXS profiles of the SMPV1 : $PC_{71}BM$ blend films processed using various post-treatment procedures displayed two features. First, a broad peak at 13.5 nm^{-1} was observed, evidence of $PC_{71}BM$ aggregation.[53] The formed $PC_{71}BM$ clusters had an isotropic orientation, also exhibiting a ring shape in the 2D GIWAXS patterns (Fig. S9, ESI†). Second, the intensity (peak area or height) of the (200) peak at a Q value of 5.9 nm^{-1} for the blend films was much lower than that of the pristine SMPV1 film. Thus, the crystallinity of the SMPV1 molecules in the blend film decreased as a result of the presence of $PC_{71}BM$ molecules; the $PC_{71}BM$ clusters were dispersed in

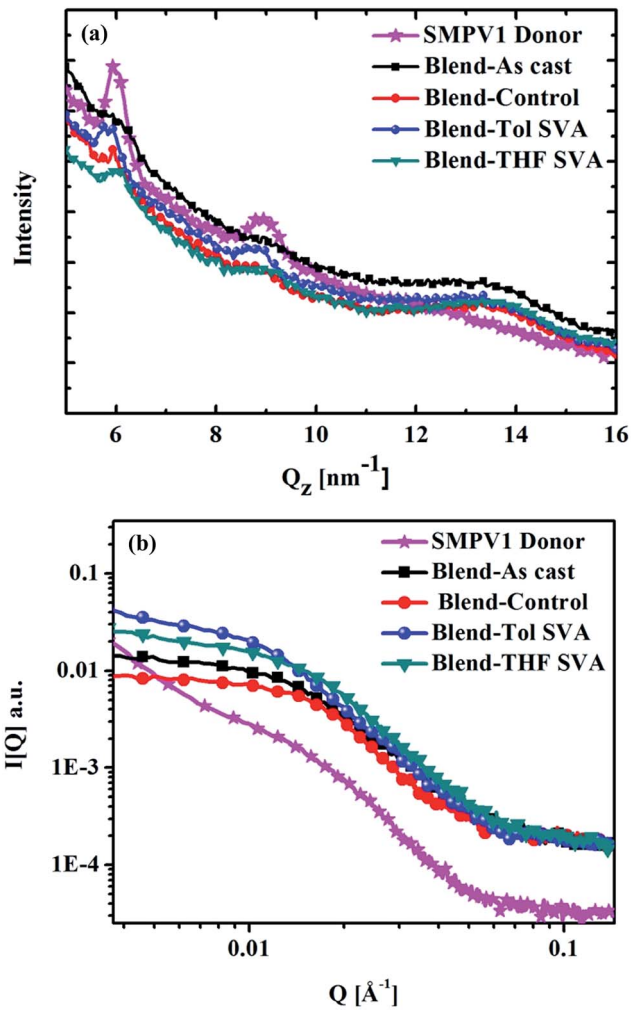

Fig. 7 (a) GIWAXS profiles and (b) corresponding GISAXS profiles of SMPV1 : $PC_{71}BM$ active layers processed from Tol and subjected to various treatment conditions.

the small molecule matrix, effectively interfering with the nucleation and growth of SMPV1 crystallites. In the GIWAXS profile of the as-cast blend film [Fig. 7(a)], the (200) and (300) diffraction peaks were the weakest among those of all the blend films, signifying the lowest degree of crystallinity of SMPV1. In contrast, the relative crystallinity, indicated by the integrated peak intensity or height of the GIWAXS (200) peak at a Q value of 5.9 nm^{-1}, of the blend films increased substantially with post-treatment in the following order: Tol-SVA > THF-SVA > control > as-cast. The GIWAXS data demonstrate that SMPV1 crystallization could be enhanced more greatly through SVA than through the combined effects of thermal annealing and use of an additive.

1D GISAXS profiles reduced from the in-plane direction (parallel to the film surface) can reveal morphological information of the inner film in a BHJ structure.[39,51] Fig. 7(b) reveals that the up-turn intensity appears in the low-Q region (0.003–0.006 $Å^{-1}$) of the GISAXS profile of the pristine SMPV1 film, implying the existence of SMPV1 domains larger than 200 nm (beyond the detection limit or the lowest Q value of 0.003 $Å^{-1}$). Upon the addition of $PC_{71}BM$, the up-turn intensity in the low-Q region of the blend films disappeared, suggesting disruption of the original SMPV1 domain into smaller domains. The GISAXS profile of the pristine SMPV1 film had a weak shoulder at 0.015 $Å^{-1}$, suggesting the existence of a few SMPV1 crystalline domains having a size of approximately 42 nm. The GISAXS profiles of the blend films featured a significant shoulder (or Guinier knee) at 0.01–0.012 $Å^{-1}$, revealing the existence of a large number of $PC_{71}BM$ clusters or domains having dimensions of 52–63 nm. Their simultaneous GIWAXS measurements revealed the $PC_{71}BM$ peak [Fig. 7(a)] and, thus, evidence that this shoulder in the GISAXS profile may be attributed to the formation of $PC_{71}BM$ clusters. The intensity of the shoulder is mainly due to the high scattering contrast of $PC_{71}BM$ clusters. It is possible that the SMPV1 crystalline domains were of similar size because of a confinement effect between the $PC_{71}BM$ and SMPV1 phases. Both SMPV1 and $PC_{71}BM$ nanodomains form a miscible distribution or bicontinuous interpenetration network, as depicted in our TEM images and in the Yang group's HRTEM data.[37] The domain larger than 200 nm is not discussed in the GISAXS analysis because this size is beyond the limitation of GISAXS.

The GISAXS profiles of the as-cast blend film and the blend film processed with thermal annealing and use of the additive (*i.e.*, the control) featured the shoulder at 0.012 $Å^{-1}$ (corresponding to domains of approximately 62 nm). Previous studies[39] using GISAXS found that thermal annealing at 70 °C had no effect on $PC_{71}BM$ clustering. Therefore, the slight discrepancy between these two GISAXS profiles, due to the additive affect, may be attributed to the dispersion of $PC_{71}BM$ clusters and SMPV1 phases or to the slight difference in the content of $PC_{71}BM$ clusters. It can be concluded, therefore, that the performance of the control blend film was better than that of the as-cast blend film mainly because of the crystallinity of SMPV1. The GISAXS profiles of the Tol- and THF-SVA blend films featured the shoulder signals at 0.01 $Å^{-1}$ (corresponding to domains of approximately 53 nm). According to the intensities of the shoulder signals, the volume fraction of the nanodomain of the Tol-SVA blend film was slightly higher than that of THF-SVA blend film, but significantly higher than that of the as-cast blend film. The large number of nanodomains in the SVA-processed blend films would, presumably, form an effective connected network for transporting the charge carriers, leading to better performance than devices based on the as-cast and control blend films.

To gain further insight into the influence of SVA treatment on the charge transport, we used the space-charge limited current (SCLC) model to determine the charge carrier mobilities. A high charge collection efficiency—and, consequently, a high FF—requires balanced carrier mobilities.[54] Fig. S10(a) and (b) and Table S10 (ESI†) present the J–V characteristics of electron- and hole-only devices prepared using the various treatment conditions. After fitting of the dark current to the SCLC model, we obtained electron and hole mobilities of the as-cast film of 4.37×10^{-5} and 1.12×10^{-5} $cm^2\ V^{-1}\ s^{-1}$, respectively, giving a charge carrier mobility ratio (μ_e/μ_h) of 3.90. After Tol- and THF-SVA treatment, higher carrier mobilities in the order of 10^{-4} $cm^2\ V^{-1}\ s^{-1}$ have been observed with μ_e/μ_h values of 1.33 and 1.64, respectively, revealing much more balanced charge transport properties. The combination of enhanced charge carrier mobility, superior morphology, and greater donor crystallinity provides a reasonable explanation for the enhanced FFs obtained after SVA treatment, leading to higher PCEs.[34,55] To confirm that our devices performances are not instantaneous, we performed stability tests for devices prepared under various treatment conditions (as-cast, control, Tol-SVA and THF-SVA). Results are shown in Fig. S11 (ESI†) in which both the as-cast and control devices lose half of their performances after 14 days of storage in a N_2-filled glovebox. For Tol- and THF-SVA, around 40% of their performances have been lost under the same storage conditions.

Conclusion

We have developed an efficient molecular solar cell processed using Tol as a halogen-free solvent. A device featuring an SMPV1 : $PC_{71}BM$ blend processed in Tol achieved a PCE of 5.4% without any post-treatment. The combined effects of thermal annealing and the use of PDMS as an additive improved the value of J_{sc} significantly, from 10.68 mA cm^{-2} (for the as-cast device) to 12.13 mA cm^{-2} (for the control device), and led to a PCE of 6.2%. For further optimization, SVA treatment was tested using various halogen-free solvents (Tol, THF, CS_2, and Hex). SVA with Tol and THF positively influenced the device performance, with significant enhancements in FFs leading to PCEs of 7.04 and 6.52%, respectively. In contrast, CS_2- and Hex-SVA treatment had negative effects on the values of J_{sc}, leading to decreases in PCEs to 5.63 and 5.56%, respectively. SVA treatment was a powerful tool for manipulating the morphologies of active layer films processed from Tol as a halogen-free solvent. Significant improvements in the FF were measured after Tol-, THF-, and CS_2-SVA treatment, primarily because of the improved morphology and phase separation. Using Tol as the halogen-free solvent led to a PCE of greater than 7% for our

optimized molecular solar cell—the highest performance reported to date. Our work paves the way toward replacing toxic halogenated solvents commonly used in the fabrication of molecular solar cells with halogen-free solvents—an important step in the large-scale industrial fabrication of organic solar cells.

Acknowledgements

We acknowledge the Taiwan Ministry of Science and Technology (102-2221-E-001-029-MY2), the Center for Sustainability Science of Academia Sinica, Taiwan (AS-103-SS-A02), and Academia Sinica, Taiwan (Career Development Award 103-CDA-M01) for financial support, and NanoCore, the Core Facilities for Nanoscience and Nanotechnology at Academia Sinica, Taiwan, for technical support.

Notes and references

1 B. Kan, M. Li, Q. Zhang, F. Liu, X. Wan, Y. Wang, W. Ni, G. Long, X. Yang, H. Feng, Y. Zuo, M. Zhang, F. Huang, Y. Cao, T. P. Russell and Y. Chen, *J. Am. Chem. Soc.*, 2015, **137**, 3886–3893.
2 Z. He, B. Xiao, F. Liu, H. Wu, Y. Yang, S. Xiao, C. Wang, T. P. Russell and Y. Cao, *Nat. Photonics*, 2015, **9**, 174–179.
3 C. J. Brabec, S. Gowrisanker, J. J. M. Halls, D. Laird, S. Jia and S. P. Williams, *Adv. Mater.*, 2010, **22**, 3839–3856.
4 D. Patra, T.-Y. Huang, C.-C. Chiang, R. O. V. Maturana, C.-W. Pao, K.-C. Ho, K.-H. Wei and C.-W. Chu, *ACS Appl. Mater. Interfaces*, 2013, **5**, 9494–9500.
5 D. Patra, C.-C. Chiang, W.-A. Chen, K.-H. Wei, M.-C. Wu and C.-W. Chu, *J. Mater. Chem. A*, 2013, **1**, 7767–7774.
6 M. E. Farahat, D. Patra, C.-H. Lee and C.-W. Chu, *ACS Appl. Mater. Interfaces*, 2015, **7**, 22542–22550.
7 P. G. Jessop, *Green Chem.*, 2011, **13**, 1391–1398.
8 Y. Chen, S. Zhang, Y. Wu and J. Hou, *Adv. Mater.*, 2014, **26**, 2744–2749.
9 G. Susanna, L. Salamandra, C. Ciceroni, F. Mura, T. M. Brown, A. Reale, M. Rossi, A. Di Carlo and F. Brunetti, *Sol. Energy Mater. Sol. Cells*, 2015, **134**, 194–198.
10 Y. Deng, W. Li, L. Liu, H. Tian, Z. Xie, Y. Geng and F. Wang, *Energy Environ. Sci.*, 2015, **8**, 585–591.
11 C. Sprau, F. Buss, M. Wagner, D. Landerer, M. Koppitz, A. Schulz, D. Bahro, W. Schabel, P. Scharfer and A. Colsmann, *Energy Environ. Sci.*, 2015, **8**, 2744–2752.
12 W. Zhao, L. Ye, S. Zhang, M. Sun and J. Hou, *J. Mater. Chem. A*, 2015, **3**, 12723–12729.
13 X. Guo, M. Zhang, C. Cui, J. Hou and Y. Li, *ACS Appl. Mater. Interfaces*, 2014, **6**, 8190–8198.
14 C.-C. Chueh, K. Yao, H.-L. Yip, C.-Y. Chang, Y.-X. Xu, K.-S. Chen, C.-Z. Li, P. Liu, F. Huang, Y. Chen, W.-C. Chen and A. K. Y. Jen, *Energy Environ. Sci.*, 2013, **6**, 3241–3248.
15 J. Zhao, Y. Li, G. Yang, K. Jiang, H. Lin, H. Ade, W. Ma and H. Yan, *Nature Energy*, 2016, **1**, 15027.
16 S. Venkatesan, Q. Chen, E. C. Ngo, N. Adhikari, K. Nelson, A. Dubey, J. Sun, V. Bommisetty, C. Zhang, D. Galipeau and Q. Qiao, *Energy Technol.*, 2014, **2**, 269–274.
17 H. Zhang, H. Yao, W. Zhao, L. Ye and J. Hou, *Adv. Energy Mater.*, 2016, 1502177.
18 J. Griffin, A. J. Pearson, N. W. Scarratt, T. Wang, A. D. F. Dunbar, H. Yi, A. Iraqi, A. R. Buckley and D. G. Lidzey, *Org. Electron.*, 2015, **21**, 216–222.
19 C.-D. Park, T. A. Fleetham, J. Li and B. D. Vogt, *Org. Electron.*, 2011, **12**, 1465–1470.
20 B. Schmidt-Hansberg, M. Sanyal, N. Grossiord, Y. Galagan, M. Baunach, M. F. G. Klein, A. Colsmann, P. Scharfer, U. Lemmer, H. Dosch, J. Michels, E. Barrena and W. Schabel, *Sol. Energy Mater. Sol. Cells*, 2012, **96**, 195–201.
21 F. Machui, S. Langner, X. Zhu, S. Abbott and C. J. Brabec, *Sol. Energy Mater. Sol. Cells*, 2012, **100**, 138–146.
22 X. Chen, X. Liu, M. A. Burgers, Y. Huang and G. C. Bazan, *Angew. Chem., Int. Ed.*, 2014, **53**, 14378–14381.
23 I. Burgués-Ceballos, F. Machui, J. Min, T. Ameri, M. M. Voigt, Y. N. Luponosov, S. A. Ponomarenko, P. D. Lacharmoise, M. Campoy-Quiles and C. J. Brabec, *Adv. Funct. Mater.*, 2014, **24**, 1449–1457.
24 B. Walker, A. Tamayo, D. T. Duong, X.-D. Dang, C. Kim, J. Granstrom and T.-Q. Nguyen, *Adv. Energy Mater.*, 2011, **1**, 221–229.
25 G. Li, Y. Yao, H. Yang, V. Shrotriya, G. Yang and Y. Yang, *Adv. Funct. Mater.*, 2007, **17**, 1636–1644.
26 G. Li, V. Shrotriya, J. Huang, Y. Yao, T. Moriarty, K. Emery and Y. Yang, *Nat. Mater.*, 2005, **4**, 864–868.
27 J. Peet, J. Y. Kim, N. E. Coates, W. L. Ma, D. Moses, A. J. Heeger and G. C. Bazan, *Nat. Mater.*, 2007, **6**, 497–500.
28 M. E. Farahat, H.-Y. Wei, M. A. Ibrahem, K. M. Boopathi, K.-H. Wei and C.-W. Chu, *RSC Adv.*, 2014, **4**, 9401–9411.
29 C. D. Wessendorf, G. L. Schulz, A. Mishra, P. Kar, I. Ata, M. Weidelener, M. Urdanpilleta, J. Hanisch, E. Mena-Osteritz, M. Lindén, E. Ahlswede and P. Bäuerle, *Adv. Energy Mater.*, 2014, **4**, 1400266.
30 K. Sun, Z. Xiao, E. Hanssen, M. F. G. Klein, H. H. Dam, M. Pfaff, D. Gerthsen, W. W. H. Wong and D. J. Jones, *J. Mater. Chem. A*, 2014, **2**, 9048–9054.
31 K. Sun, Z. Xiao, S. Lu, W. Zajaczkowski, W. Pisula, E. Hanssen, J. M. White, R. M. Williamson, J. Subbiah, J. Ouyang, A. B. Holmes, W. W. H. Wong and D. J. Jones, *Nat. Commun.*, 2015, **6**, 6013.
32 H. C. Liao, C. S. Tsao, Y. C. Huang, M. H. Jao, K. Y. Tien, C. M. Chuang, C. Y. Chen, C. J. Su, U. S. Jeng, Y. F. Chen and W. F. Su, *RSC Adv.*, 2014, **4**, 6246–6253.
33 B. Kan, Q. Zhang, M. Li, X. Wan, W. Ni, G. Long, Y. Wang, X. Yang, H. Feng and Y. Chen, *J. Am. Chem. Soc.*, 2014, **136**, 15529–15532.
34 J.-L. Wang, Q.-R. Yin, J.-S. Miao, Z. Wu, Z.-F. Chang, Y. Cao, R.-B. Zhang, J.-Y. Wang, H.-B. Wu and Y. Cao, *Adv. Funct. Mater.*, 2015, **25**, 3514–3523.
35 G. De Luca, E. Treossi, A. Liscio, J. M. Mativetsky, L. M. Scolaro, V. Palermo and P. Samori, *J. Mater. Chem.*, 2010, **20**, 2493–2498.
36 J. D. Zimmerman, X. Xiao, C. K. Renshaw, S. Wang, V. V. Diev, M. E. Thompson and S. R. Forrest, *Nano Lett.*, 2012, **12**, 4366–4371.

37 Y. Liu, C.-C. Chen, Z. Hong, J. Gao, Y. Yang, H. Zhou, L. Dou, G. Li and Y. Yang, *Sci. Rep.*, 2013, **3**, 3356.
38 G. G. Malliaras, J. R. Salem, P. J. Brock and C. Scott, *Phys. Rev. B: Condens. Matter Mater. Phys.*, 1998, **58**, R13411–R13414.
39 Y.-C. Huang, C.-S. Tsao, T.-Y. Huang, H.-C. Cha, D. Patra, C.-J. Su, U. S. Jeng, K.-C. Ho, K.-H. Wei and C.-W. Chu, *J. Phys. Chem. C*, 2015, **119**, 16507–16517.
40 H.-C. Liao, C.-S. Tsao, T.-H. Lin, M.-H. Jao, C.-M. Chuang, S.-Y. Chang, Y.-C. Huang, Y.-T. Shao, C.-Y. Chen, C.-J. Su, U. S. Jeng, Y.-F. Chen and W.-F. Su, *ACS Nano*, 2012, **6**, 1657–1666.
41 A. R. b. Mohd Yusoff, D. Kim, F. K. Schneider, W. J. da Silva and J. Jang, *Energy Environ. Sci.*, 2015, **8**, 1523–1537.
42 A. Viterisi, F. Gispert-Guirado, J. W. Ryan and E. Palomares, *J. Mater. Chem.*, 2012, **22**, 15175–15182.
43 F. Liu, Y. Gu, X. Shen, S. Ferdous, H.-W. Wang and T. P. Russell, *Prog. Polym. Sci.*, 2013, **38**, 1990–2052.
44 G. L. Schulz, M. Lobert, I. Ata, M. Urdanpilleta, M. Linden, A. Mishra and P. Bauerle, *J. Mater. Chem. A*, 2015, **3**, 13738–13748.
45 J. Miao, H. Chen, F. Liu, B. Zhao, L. Hu, Z. He and H. Wu, *Appl. Phys. Lett.*, 2015, **106**, 183302.
46 A. K. K. Kyaw, D. H. Wang, C. Luo, Y. Cao, T.-Q. Nguyen, G. C. Bazan and A. J. Heeger, *Adv. Energy Mater.*, 2014, **4**, 1301469.
47 L. A. Perez, K. W. Chou, J. A. Love, T. S. van der Poll, D.-M. Smilgies, T.-Q. Nguyen, E. J. Kramer, A. Amassian and G. C. Bazan, *Adv. Mater.*, 2013, **25**, 6380–6384.
48 A. Sharenko, M. Kuik, M. F. Toney and T.-Q. Nguyen, *Adv. Funct. Mater.*, 2014, **24**, 3543–3550.
49 B. A. Collins, J. R. Tumbleston and H. Ade, *J. Phys. Chem. Lett.*, 2011, **2**, 3135–3145.
50 W. Chen, M. P. Nikiforov and S. B. Darling, *Energy Environ. Sci.*, 2012, **5**, 8045–8074.
51 C.-Y. Chen, C.-S. Tsao, Y.-C. Huang, H.-W. Liu, W.-Y. Chiu, C.-M. Chuang, U. S. Jeng, C.-J. Su, W.-R. Wu, W.-F. Su and L. Wang, *Nanoscale*, 2013, **5**, 7629–7638.
52 W. Chen, T. Xu, F. He, W. Wang, C. Wang, J. Strzalka, Y. Liu, J. Wen, D. J. Miller, J. Chen, K. Hong, L. Yu and S. B. Darling, *Nano Lett.*, 2011, **11**, 3707–3713.
53 Y.-W. Su, C.-M. Liu, J.-M. Jiang, C.-S. Tsao, H.-C. Cha, U. S. Jeng, H.-L. Chen and K.-H. Wei, *J. Phys. Chem. C*, 2015, **119**, 3408–3417.
54 Z. He, C. Zhong, X. Huang, W.-Y. Wong, H. Wu, L. Chen, S. Su and Y. Cao, *Adv. Mater.*, 2011, **23**, 4636–4643.
55 P. W. M. Blom, V. D. Mihailetchi, L. J. A. Koster and D. E. Markov, *Adv. Mater.*, 2007, **19**, 1551–1566.